© 2024. Published by The Company of Biologists Ltd | Journal of Cell Science (2024) 137, jcs261303. doi:10.1242/jcs.261303

RESEARCH ARTICLE

SPECIAL ISSUE: CELL AND TISSUE POLARITY

PALS1 is a key regulator of the lateral distribution of tight junction proteins in renal epithelial cells

Ann-Christin Groh[1,*], Annika Möller-Kerutt[1,*], Kevin Gilhaus[1], Verena Höffken[1], Pavel Nedvetsky[2], Simon Kleimann[1], Malina Behrens[1], Sujasha Ghosh[3], Uwe Hansen[4], Michael P. Krahn[2], Klaus Ebnet[5], Hermann Pavenstädt[1], Alexander Ludwig[3] and Thomas Weide[1,‡]

ABSTRACT

The evolutionarily conserved apical Crumbs (CRB) complex, consisting of the core components CRB3a (an isoform of CRB3), PALS1 and PATJ, plays a key role in epithelial cell–cell contact formation and cell polarization. Recently, we observed that deletion of one *Pals1* allele in mice results in functional haploinsufficiency characterized by renal cysts. Here, to address the role of PALS1 at the cellular level, we generated CRISPR/Cas9-mediated PALS1-knockout MDCKII cell lines. The loss of PALS1 resulted in increased paracellular permeability, indicating an epithelial barrier defect. This defect was associated with a redistribution of several tight junction-associated proteins from bicellular to tricellular contacts. PALS1-dependent localization of tight junction proteins at bicellular junctions required its interaction with PATJ. Importantly, reestablishment of the tight junction belt upon transient F-actin depolymerization or upon Ca^{2+} removal was strongly delayed in PALS1-deficient cells. Additionally, the cytoskeleton regulator RhoA was redistributed from junctions into the cytosol under PALS1 knockout. Together, our data uncover a critical role of PALS1 in the coupling of tight junction proteins to the F-actin cytoskeleton, which ensures their correct distribution along bicellular junctions and the formation of tight epithelial barrier.

KEY WORDS: PALS1, Cell junction, Cell polarity, Renal diseases, Renal epithelia, Tight junction

INTRODUCTION

Apicobasal cell polarization establishes an asymmetric distribution of lipids and proteins in the plasma membrane and forms the basis for the physiological role of numerous epithelia in mammalian organs. Studies from the past two decades in *Drosophila melanogaster*, in the zebrafish *Danio rerio* and in mammalian cell cultures have demonstrated the essential role of the evolutionarily conserved Crumbs (CRB) complex in epithelial cell polarity and epithelial tissue morphogenesis (Martin et al., 2021; Thompson et al., 2013). The CRB core complex consists of the name-giving type I transmembrane protein Crumbs (in mammals mainly CRB3a; an isoform of CRB3), lin-7 homolog C (LIN7c), protein associated with LIN7c (PALS1) and PALS1-associated tight junction protein (PATJ) (Martin et al., 2021; Pieczynski and Margolis, 2011). Recently, it has been shown that the CRB complex components CRB3a, PATJ and PALS1 localize directly apical to the tight junction (TJ) in a novel compartment called the vertebrate marginal zone (VMZ) (Mangeol et al., 2022; Tan et al., 2020). Several *in vitro* studies have identified an essential role for mammalian CRB3, PALS1 and PATJ in TJ formation (Fogg et al., 2005; Lemmers et al., 2004; Michel et al., 2005; Straight et al., 2004; Tan et al., 2020; van Rossum et al., 2006; Wang et al., 2007). In addition, PALS1, PATJ and CRB3 are required for lumen formation in 3D mammalian epithelial cell cultures (Schlüter et al., 2009; Shin et al., 2005; Straight et al., 2004). Taken together, this shows that the CRB complex is a critical regulator of epithelial tissue morphogenesis.

Cell polarization and the formation of cell contacts are of outstanding importance for mammalian kidneys, particularly for renal nephron epithelia. The physiological function of various tubular nephron epithelia depends on the asymmetric distribution of numerous channels and transporters to regulate the resorption and recycling of nutrients, as well as on the formation of TJs to regulate the salt and ion homeostasis and to concentrate the primary ultrafiltrate into excretable urine.

Several studies indicate an important role for the CRB complex in kidney function and imply that dysfunction of CRB core components might act as a causative or aggravating factor for renal diseases. For instance, mice lacking CRB3 or LIN7c develop cysts in the renal tubules of the kidneys (Charrier et al., 2015; Olsen et al., 2007; Whiteman et al., 2014). In addition, heterozygous PALS1-knockout (KO) mice with a reduced PALS1 expression in all nephron epithelia (Weide et al., 2017) develop proteinuria and form numerous cysts leading to death within the first 2 months after birth (Berghaus et al., 2022; Weide et al., 2017). Remarkably, in the case of PALS1, the loss of only one allele is sufficient to cause this phenotype, indicating a crucial and dose-dependent function of PALS1 in renal epithelial cells (Weide et al., 2017). However, it remains unclear whether reduced PALS1 levels lead to defects in cell polarization or rather affect the formation of cell–cell contacts between the epithelial cells of the nephron.

In this study, we analyzed the role of PALS1 in the formation of AJs and TJs in Madin Darby canine kidney (MDCKII, hereafter just called MDCK) cells in which both *PALS1* alleles were inactivated using CRISPR/Cas9. These cells show moderate defects in cell polarization but exhibit dramatically increased paracellular permeability. Strikingly,

---

[1]University Hospital of Münster (UKM), Internal Medicine D (MedD), Department Molecular Nephrology, Albert-Schweitzer-Campus 1 Building A14, 48149 Münster, Germany. [2]University Hospital of Münster (UKM), Internal Medicine D (MedD), Medical Cell Biology, Albert-Schweitzer-Campus 1 Building A14, 48149 Münster, Germany. [3]School of Biological Sciences and NTU Institute of Structural Biology (NISB), Nanyang Technological University, 60 Nanyang Drive, 637551 Singapore City, Singapore. [4]University Hospital of Münster, Institute of Musculoskeletal Medicine (IMM), Head Core Facility Electron Microscopy, Domagkstraße 3, 48149 Münster, Germany. [5]Institute-associated Research Group "Cell adhesion and cell polarity", Institute of Medical Biochemistry, Center for Molecular Biology of Inflammation (ZMBE), University of Münster, Von-Esmarch-Straße 56, 48149 Münster, Germany.
*These authors contributed equally to this work

‡Author for correspondence (weidet@uni-muenster.de)

K.E., 0000-0002-0417-7888; A.L., 0000-0002-0696-5298; T.W., 0000-0002-2707-665X

Handling Editor: David Bryant
Received 3 May 2023; Accepted 4 December 2023

several TJ components such as ZO-1 and ZO-3 (also known as TJP1 and TJP3, respectively) and occludin as well as the PALS1-binding partner PATJ are lost from bicellular TJs in *PALS1* KO cells. Moreover, reestablishment of the tight junctional belt after transient F-actin depolymerization by Latrunculin A was significantly delayed in the absence of PALS1. Thus, our data provide novel evidence that PALS1 regulates the barrier function in MDCK cells by controlling the lateral distribution of TJ components and its coupling to the actin cytoskeleton.

RESULTS

The knockout of PALS1 in MDCK cells causes severe barrier defects

To ensure the complete absence of PALS1, we established MDCK KO cells by CRISPR/Cas9 and selected a target sequence within the exon 7 of the canine *PALS1* gene, encoding the PALS1 PDZ domain (Fig. S1A). The two selected knockout clones KO1 and KO2 showed no expression of the two PALS1 splice variants (Fig. 1A). Immunofluorescence (IF) analyses confirmed the complete absence of PALS1 at cell–cell junctions (Fig. 1B).

To test whether loss of PALS1 affects the barrier properties of MDCK cells, we measured the trans-epithelial electrical resistance (TEER) of MDCK wild-type (WT) and PALS1 KO cells. TEER measurements are suitable to analyze the tightness of cell–cell junctions and the ion transport properties (pore pathway) of epithelial cells. We first compared TEER of WT and PALS1 KO cells during the establishment of epithelial monolayers on Transwell filters. Whereas WT cells established peak TEER values around 3 days post seeding, the typical TEER peak was not observed in KO cells, in line with previous studies (Straight et al., 2004; Fig. S1B). Next, we tested TEER development using the well-established Ca^{2+} switch assay. The withdrawal of Ca^{2+} ions from the medium led to a complete disruption of cell–cell contacts in MDCK monolayers and collapse of the TEER. The effect was reversible, as the subsequent addition of Ca^{2+} to the medium results in the re-formation of cell–cell contacts and TEER. TEER measurements during the Ca^{2+} switch assay revealed strongly reduced TEER values upon withdrawal of Ca^{2+} in both MDCK WT and PALS1 KO cell monolayers. WT cells completely re-established the high TEER values within 24 h after Ca^{2+} re-addition, whereas PALS1 KO cells showed no TEER increase during this time period (Fig. S1C). This demonstrates loss of TJ resistance in PALS1 KO cells.

The altered TEER in PALS1 KO cells grown in 2D monolayers suggested differences in the formation or functionality of cell–cell junctions. To investigate whether PALS1 KO caused the permeability to be increased for ions only or for larger molecules as well, we analyzed MDCK WT and PALS1 KO cells using a 3D cyst permeability assay. MDCK cells embedded in extracellular matrix (ECM) form 3D spherical cysts with a single apical lumen. These cysts consist of a layer of apicobasally polarized cells. 3D MDCK cysts share many properties with *in vivo* epithelia and are an excellent *in vitro* model for studying polarity and cell–cell contact formation and integrity (Elia and Lippincott-Schwartz, 2009). To address the function of PALS1 in this system, the accumulation of fluorescently labeled dextran (Alexa Fluor 647, 10 kDa; FITC, 3–5 kDa) in the cyst lumens was analyzed over time. Although neither single-lumen nor multiple-lumen WT cysts showed any accumulation of labeled dextran in their lumen over the time period of 15 min, dextran intraluminal accumulation in PALS1 KO cyst was evident within the first two minutes of dextran administration and increased over time (Fig. 1C,D; Fig. S1D,E). These data indicate that PALS1 regulates the establishment of the paracellular ion barrier (pore pathway) as well as the barrier for small solutes (leak pathway). Given that WT1 and WT2 as well as KO1 and KO2 showed identical phenotypes, from now on only data from WT1 (denoted WT) and KO1 (denoted KO) are presented as representatives of each phenotype.

Next, we analyzed the cell–cell junctions in 3D cysts for potential changes in their structure by transmission electron microscopy (TEM). The apical regions of cell–cell contacts, which contain the TJs, appeared more diffuse and less electron-dense in PALS1 KO cells compared to in the WT cells. In contrast, desmosomal structures showed no obvious differences between WT and PALS1 KO cells in 3D cysts, indicating that PALS1 regulates the structure of cell–cell junctions in the apical region of epithelial cells (Fig. 1E).

PALS1 depletion results in altered distribution of TJ proteins at bicellular junctions

The increased permeability of cell–cell contacts in PALS1 KO cysts and the ultrastructural changes in the apical region of cell–cell contacts of KO cells found by TEM argue for changes in TJ organization and function. To test this, we first investigated the distribution of ZO-1 as a marker for TJs, and E-cadherin as a marker for adherens junctions (AJs) in WT and KO cysts.

In the cells lining the cysts, ZO-1 showed an apical distribution facing the lumen. E-cadherin, on the other hand, was found basolaterally between the individual cells of the cysts. This was the case both for WT and PALS1 KO cells, and was observed in single lumen cysts as well as in cysts with multiple lumens (Fig. S2A). Of note, both WT and PALS1 KO cells formed cysts with single, multiple and no lumen. However, multiple- and no-lumen cysts were more prevalent in PALS1 KO cell lines (Fig. S2B), in agreement with previous work using PALS1 KD MDCK cell lines (Straight et al., 2004).

Strikingly, in cysts, PALS1 deficiency resulted in ZO-1 positive ‘spike-like’ elongations at tricellular junctions, which was accompanied by a discontinuous ZO-1 pattern in bicellular junctions (Fig. 2A, middle row). These spikes were absent in the MDCK WT cysts (Fig. 2A, upper row).

To verify the specificity of the CRISPR/Cas9-mediated PALS1 KO we re-expressed HALO-tagged PALS1 in PALS1 KO cell lines. PALS1 KO cysts that expressed PALS1–HALO fusion proteins re-established the continuous ZO-1 distribution along bi- and tricellular junctions in 3D. Spike-like elongations at tricellular junctions were not observed (Fig. 2A, lower panel).

Next, we analyzed the distribution of TJ and AJ proteins in 2D monolayers. MDCK WT cells showed a ‘chicken-wire-like’ distribution of E-cadherin and ZO-1 (Fig. 2B). In PALS1 KO cells, ZO-1 disappeared from bicellular junctions, leading to a ‘dot-like’ pattern of ZO-1 that was caused by strong ZO-1 signals at the tricellular junctions (Fig. 2B). The TJ protein occludin also exhibited a reduced intensity along bicellular junctions in PALS1 KO cells (Fig. S3A). By contrast, E-cadherin (Fig. 2B) and the lateral membrane protein JAM-A (also known as F11R) (Iden et al., 2012; Martìn-Padura et al., 1998) (Fig. S3B) showed a normal chicken-wire-like distribution both in WT and PALS1 KO cells.

The strong decrease of TJ proteins at bicellular junctions prompted us to analyze the vertical distribution of ZO-1 and E-cadherin in polarized 2D monolayers (*z*-axis). To this end, we determined the ratio of the lateral E-cadherin and ZO-1 signals over the total junctional length (length of ZO-1 plus E-cadherin signals). The analysis revealed no overt changes in the lateral length of E-cadherin in polarized WT and PALS1 KO monolayers. However, PALS1 KO cells showed a small but significant elongation of the ZO-1 signal (Fig. S4).

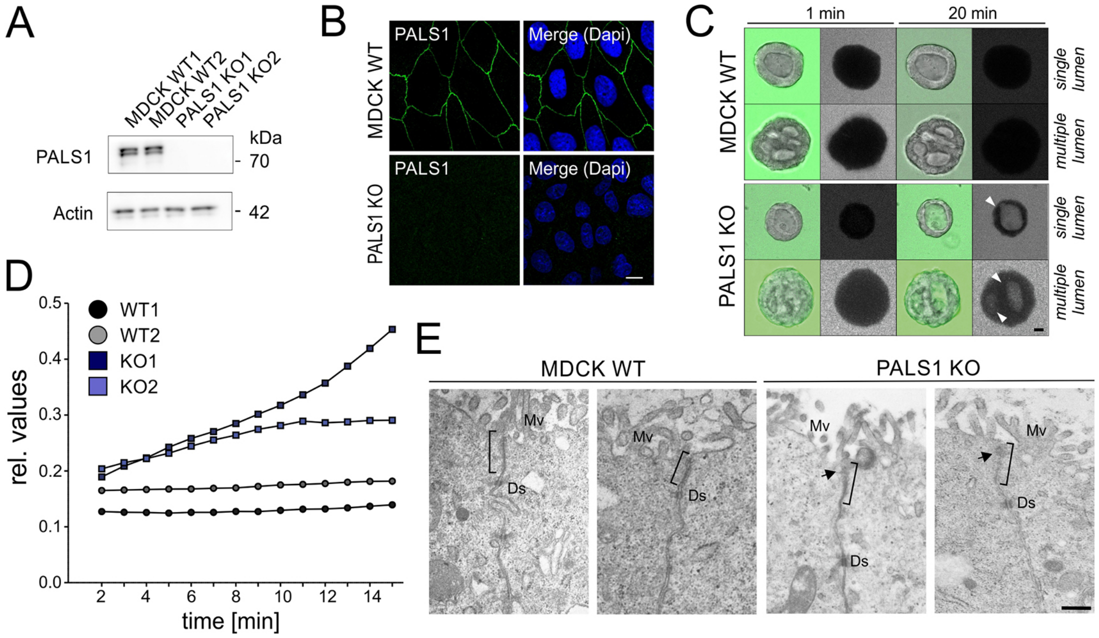

Fig. 1. PALS1 KO cell lines show a severe permeability defect. (A) Western blot analyses of WT and PALS1 KO cell clones. Lysates of cells WT1 or cells that passed through the entire CRISPR/Cas9 process without changing the *PALS1* gene sequence (WT2) and both PALS1 KO clones (KO1 and KO2) were analyzed for expression of PALS1. Actin served as loading controls. No PALS1 expression was detectable in PALS1-deficient samples. (B) Immunofluorescence (IF) analyses of WT and PALS1 KO cells. In contrast to the WT cells PALS1 KO cells show the complete absence of PALS1 at cellular junctions. Scale bar: 10 µm. (C) Permeability assays. Labeled dextran (4 kDa) was used to analyze the permeability of WT and PALS1 KO cysts. No uptake was detectable in either single- or multiple-lumen WT cysts. However, the luminal signal intensity was increased in single- and multiple-lumen PALS1 KO cysts. Arrowheads highlight the lumen of the cyst. The permeability assays were performed with simultaneous detection of both dextran samples: FITC-labeled 4 kDa dextran and Alexa Fluor 647-labeled 10 kDa dextran. The results for Alexa Fluor 647–dextran are summarized in Fig. S1D. Scale bar: 10 µm. (D) Time course of the permeability assays (*N*=3) for cysts (*n*=50) derived from two independent WT (WT1, WT2) and PALS1 KO (KO1, KO2) cell lines. Signal intensity (relative value) analysis over time within the lumen was normalized to the surrounding signal in the medium. (E) TEM images of apical junction regions (black parentheses) of WT (left) and PALS1 KO (right) cells. In WT cells, electron dense and clearly structured apical junctional regions, which contain the TJs, are found, whereas in PALS1 KO cells, this region is less electron-dense and more diffuse (arrows). Ds, desmosome; Mv, microvilli. Scale bar: 1 µm. Images in A, B and E are representative of *n*≥3 experiments.

We also analyzed PALS1 KO cells expressing the PALS1–HALO fusion proteins in 2D monolayers. Indeed, cells expressing the PALS1–HALO fusion protein re-established the continuous distribution of endogenous ZO-1 in bi- and tri-cellular junctions (Fig. 2C). Bicellular contacts between PALS1–HALO-positive cells and cells without a detectable PALS1–HALO expression maintained a disrupted ZO-1 distribution. Thus, PALS1 expression is required for the continuous distribution of ZO-1 in 2D and 3D cultures of epithelial cells.

The continuous lateral distribution of TJ proteins is directly linked to cellular PALS1 expression

Data shown in the Fig. 2C indicate that the expression of PALS1 only in one cell of a cell–cell contact is unable to trigger full TJ formation in the adjoining cell. To investigate the impact of PALS1 on TJ proteins of neighboring cells in more detail, we used co-culture monolayers (1:1) of MDCK WT and PALS1 KO cells and performed IF studies with antibodies against PALS1, ZO-1 (Fig. 3A), E-cadherin, occludin and claudin 1 (Fig. S5).

At bicellular contacts, the highest signal intensity of ZO-1 was observed between junctions of two WT cells (WT–WT). Cell junctions between one WT and one KO (WT–KO) cell showed reduced signal intensities and the contacts of two KO cells (KO–KO) showed the lowest levels (Fig. 3A,B). In comparison to the expected stepwise decrease of the PALS1 signal (WT–WT versus WT–KO and KO–KO, respectively), the reduction in the ZO-1 signal in WT–KO and KO–KO contacts was moderate, with average values not below 80% of those of the WT–WT contacts (Fig. 3C). IF studies of co-cultures grown on glass coverslips confirmed our observations on Transwell filters and again showed a reduction in TJ proteins (ZO-1, occludin and claudin 1) at bicellular junctions (Fig. S5). For the AJ protein E-cadherin, we could not observe an alteration at the bicellular junctions (Fig. S5). In contrast, tricellular junctions shared by KO cells (KO–KO–KO) showed the strongest ZO-1 signal intensity. The intensity in mixed junctions (WT–WT–KO and WT–KO–KO, respectively) was in between the values of the homogenous tricellular junctions composed only of WT or KO cells (Fig. 3D). Together, these data suggest that the continuous distribution of ZO-1 in bicellular pools is directly linked to the PALS1 expression level within a cell–cell contact.

PALS1 controls the expression and localization of PATJ at TJs

Membrane binding of PALS1 is mediated by its interaction with PATJ (Roh et al., 2002a). We therefore wondered whether the interaction of PALS1 with PATJ is needed for and linked to the proper distribution of TJ proteins. To address this, we expressed two PALS1 mutants with a C-terminal GFP tag in PALS1 KO cells (Fig. S6A). One mutant lacked the N-terminal evolutionarily conserved region (ECR), which mediates binding to PAR6 [ΔECR:, amino acids (aa) 118–675; Hurd et al., 2003; Penkert et al., 2004; Wang et al., 2004]. The other mutant additionally lacked the N-terminal L27 domain (L27N), which binds to PATJ (ΔECR+L27N, aa 178–675) (Roh et al., 2002a). Full-length

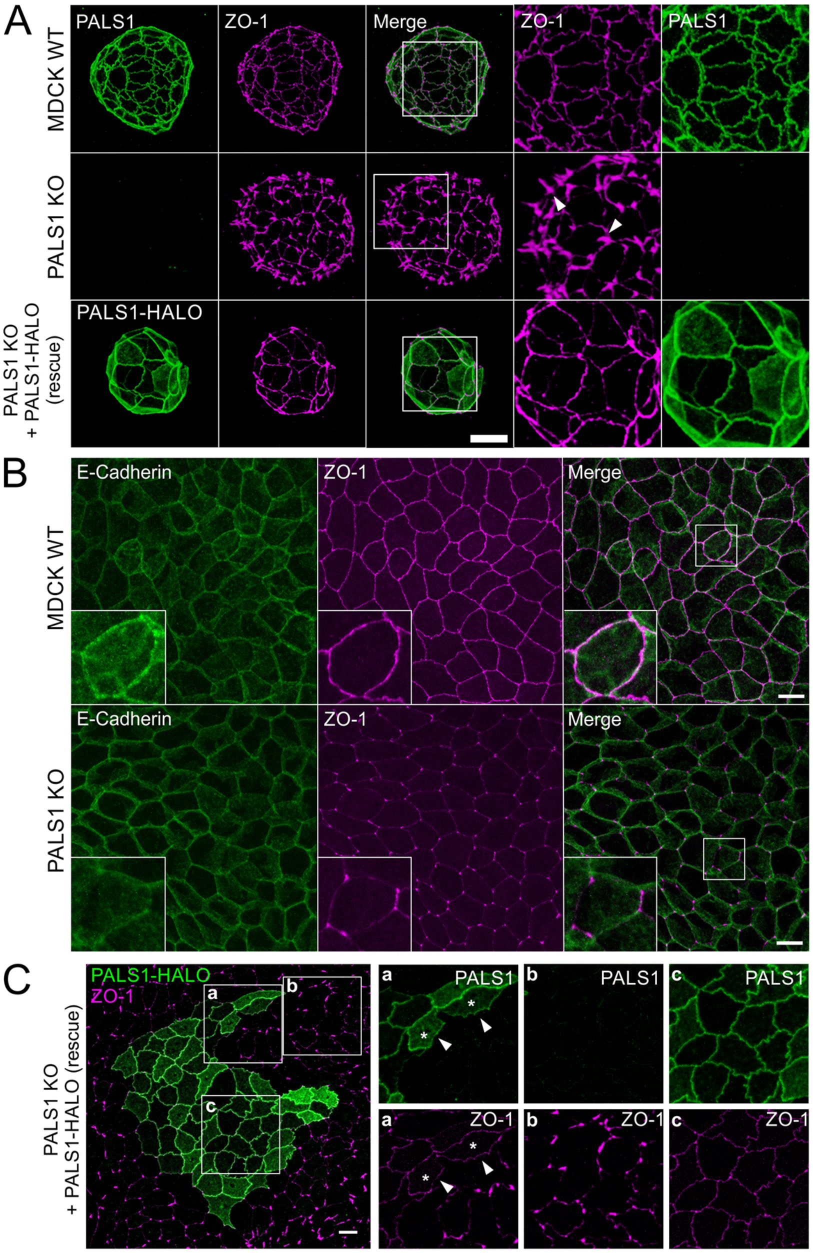

Fig. 2. PALS1 depletion alters the lateral distribution of the TJ protein ZO-1. (A) IF analyses of 3D cysts. In comparison to WT cysts, cysts from PALS1 KO cells show a spike-like distribution of ZO-1 (magenta, arrowheads), accompanied by a discontinued distribution of the ZO-1 signal at bicellular junctions. Rescue cysts that express full-length PALS1 fused to a HALO tag (PALS1–HALO) lose their spike-like ZO-1 misdistribution phenotype. Brightness and contrast were increased equally for all images. Scale bar: 10 µm (B) IF analyses using E-cadherin and ZO-1. The distribution of E-cadherin (green) showed no obvious differences in 2D cultures of WT and PALS1 KO cells. In contrast, the distribution of ZO-1 (magenta) in PALS1 KO cells shows a strong decrease of the signal in bicellular contacts, which is accompanied by an accumulation of this TJ protein in tricellular contacts. Scale bars: 10 µm. (C) IF analyses of polarized PALS1 KO cells plus cells rescued by the expression of a PALS1–HALO. Cells expressing the PALS1-HALO rescue construct (green patches) show a complete restoration of the ZO-1 dot-like mislocalization phenotype of PALS1 KO cells. Detail a: border area between rescued and non-rescued PALS1 monolayer; detail b: non-rescued area; detail c: full-rescued area. Scale bars: 10 µm. Images representative of *n*=4 experiments.

PALS1 fused to GFP (PALS1–GFP full length) was used as a positive control. Transient transfection of constructs encoding these PALS1–GFP fusion proteins in PALS1 KO cells showed that only GFP-tagged full-length PALS1 and the ΔECR deletion mutant localized to cell junctions and were able to re-establish a continuous ZO-1 distribution. The ΔECR+L27N deletion mutant, lacking the first 177 aa, failed to localize to TJs and showed a diffuse cytoplasmic localization (Fig. S6B). These data indicate that the interaction between PALS1 and PATJ is essential for proper TJ distribution.

IF studies and western blot analyses were used to investigate to what extent PALS1 determines the intracellular localization and expression of PATJ. We observed a strong colocalization of the TJ protein ZO-1 with PALS1, PATJ and the PATJ-binding partner ZO-3 in bi- and tri-cellular junctions of WT cells (Fig. 4). For PALS1 KO cells, the IF studies revealed a strong reduction of junctional PATJ indicating that PALS1 regulates the junctional level of PATJ. Remaining PATJ and ZO-3 showed a dot-like pattern, that strongly overlapped with that of ZO-1 (Fig. 4A). Western blot analyses of MDCK WT and PALS1 KO cells revealed a strong reduction of PATJ in PALS1 KO cells, whereas LIN7c and actin expression levels remain unchanged. TJ proteins ZO-1 and ZO-3 showed slightly reduced expression levels in PALS1 KO lysates, in contrast to what was seen for E-cadherin, which showed a similar expression in WT and KO cells (Fig. 4B). Strikingly, expression of the PALS1–HALO fusion protein in PALS1 KO cells resulted in the re-establishment of the endogenous PATJ expression levels as well as of its junctional localization (Fig. 4C).

To clarify to what extent these effects are dose dependent, we analyzed PALS1 knockdown (KD) cell lines stably expressing a PALS1 shRNA (Fig. S7). PALS1 KD cells showed a strong reduction in PALS1 and PATJ expression. Residual endogenous PALS1 in PALS1 KD cells showed a weak punctate pattern that was different to the continuous belt-like staining seen in WT cells (Fig. S7A). TJ

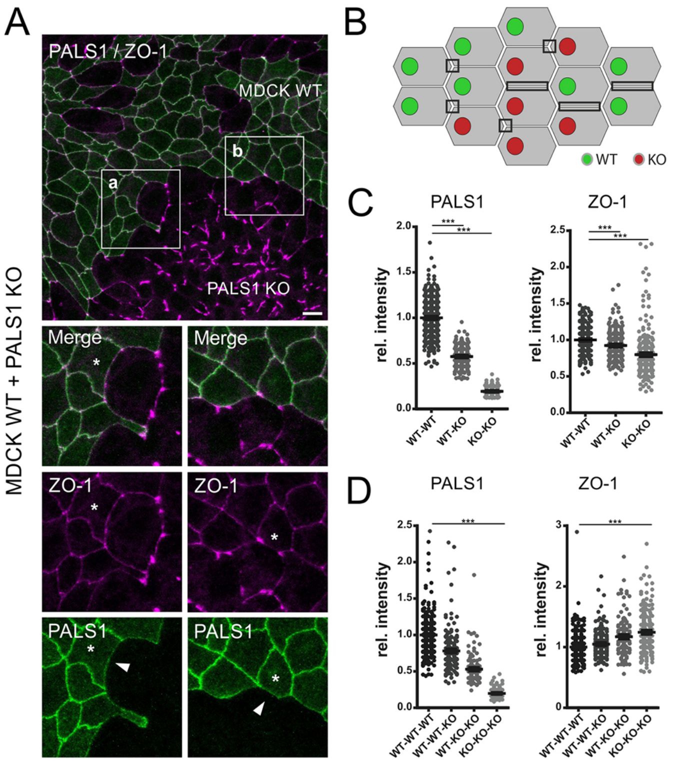

Fig. 3. The continuous lateral ZO-1 distribution is directly linked to cellular PALS1 expression. (A) Distribution of PALS1 (green) and ZO-1 (magenta) in 1:1 mixed co-cultures of WT and PALS1 KO cells. Images show a maximum intensity projection. Brightness and contrast were increased equally for all images. Asterisk highlights a WT cell; arrowheads highlight joined WT–KO bicellular junctions. Scale bar: 10 µm (B) Scheme of co-cultured WT (green) and PALS1 KO cells (red). Co-culture monolayers establish different types of bi- and tri-cellular contacts. Bicellular contacts include three possible variants (WT–WT, WT–KO and KO–KO) and tricellular contacts four (WT–WT–WT, WT–WT–KO, WT–KO–KO and KO–KO–KO). (C,D) Quantitative analyses of the relative intensity at bicellular (C) and tricellular junctions (D) for either PALS1 or ZO-1. Signals were measured using a region of interest (ROI) with a defined size. Intensities were normalized to the mean intensity of bi- and tri-cellular junctions of the WT (WT–WT and WT–WT–WT, respectively). (C) Quantitative analyses of bicellular junctions. The relative intensity of PALS1 and ZO-1 revealed a significant decrease in signal intensity from WT–WT (*n*=374) over WT–KO (*n*=221) to KO–KO (*n*=270) contacts. All possible cell–cell contact formations were tested for significance and show values below *P*≤0.001 (***; Kruskal–Wallis-test with the Dunn's correction). (D) Quantitative analyses of tricellular junctions. The relative intensity of PALS1 is significantly decreased. The more KO cells are part of a tricellular junction the lower the PALS1 signal. Vice versa, ZO-1 signal significantly increases in case that at least one PALS1 KO cell contributes to a tricellular junction and is strongest in tricellular junctions that completely lack PALS1 (D, right graph). WT–WT–WT (*n*=414) versus KO–KO–KO (*n*=214) combinations were highly significant, with *P*-values below *P*≤0.001 (***; Kruskal–Wallis-test with the Dunn's correction). The other contact formation combinations, WT-WT-WT versus WT-WT-KO (*n*=214) and WT-KO-KO (*n*=136) versus KO-KO-KO showed a similar trend in this direction but with *P*>0.05 (Kruskal–Wallis-test with the Dunn's correction).

proteins ZO-1 and ZO-3 were strongly reduced along bicellular junctions and showed a dot-like pattern in tricellular junctions, similar or identical to PALS1 KO cells. Moreover, co-cultures of PALS1 KD cells and MDCK cells expressing a control shRNA showed a strong decrease in PATJ and occludin levels at bicellular TJs. PALS1 KD cells stably expressing a shRNA-resistant PALS1–GFP fusion protein rescued the expression and the normal bicellular TJ distribution of endogenous PATJ (Fig. S7). Together, these data indicate that the expression of PALS1 at WT levels is crucial for the continuous lateral distribution of PATJ and a range of bona fide TJ proteins at bicellular TJs.

Latrunculin A evokes actin depolymerization phenocopies PALS1 deficiency

The data summarized in Figs 2–4 indicate that PALS1 acts upstream of TJ proteins. However, it remains unclear how PALS1, perhaps in concert with PATJ, orchestrates the lateral distribution of TJ proteins. Previous studies have identified a connection between F-actin and the ZO proteins (Belardi et al., 2020; Fanning and Anderson, 2009; Fanning et al., 2002; Odenwald et al., 2017; Rouaud et al., 2020). Moreover, it is well established that F-actin polymerization and actomyosin-mediated contractility regulate TJ formation and the permeability properties of epithelia (Belardi et al., 2020; Ivanov et al., 2005; Van Itallie et al., 2009, 2015).

We therefore treated WT and PALS1 KO cells with Latrunculin A (LatA). The LatA toxin binds to monomeric G-actin and inhibits its polymerization into F-actin oligomers, thereby affecting the self-assembly of G-actin into F-actin. In fully polarized MDCK WT cells, LatA treatment for 4 h resulted in the depolymerization of F-actin, leading to irregular (phalloidin-positive) F-actin accumulation inside the cytosol of cells and a dot-like pattern along the bicellular TJs. (Fig. 5). Junctional F-actin-positive dots were also positive for the polarity proteins PALS1 and PATJ (Fig. 5A,B), as well as the TJ proteins ZO-1 and ZO-3 (Fig. 6A,B). In almost every case, the dots were also found at tricellular regions of the TJs. In PALS1 KO cells, LatA had a similar effect – LatA-resistant F-actin pools colocalized with ZO-1 and ZO-3 dots along bicellular TJs (Fig. 6). Thus, the dot-like pattern of TJ proteins in LatA-treated MDCK WT cells strongly resembled the distribution of TJ proteins in untreated PALS1 KO cells.

F-actin re-polymerization-induced elongation of TJ protein aggregates depends on PALS1

To investigate whether F-actin re-polymerization-induced elongation of junctional TJ protein requires PALS1, we performed LatA-washout experiments with WT and KO cells. For this, we treated cells for 4 h with LatA (Fig. 7), removed the toxin and analyzed the cells 10 min or 60 min after the LatA washout. After the LatA washout in WT cells, the dot-like pattern disappeared, and F-actin as well as ZO-1 re-assembled stepwise within 60 min in the typical chicken-wire-like pattern (Fig. 7A). In PALS1 KO cells, LatA washout also led to the reestablishment of the circumferential F-actin belt, but – unlike in WT cells – without the corresponding formation of a continuous lateral distribution of TJ proteins along bicellular contacts (Fig. 7B).

To evaluate the effects of the LatA-washout assays, we analyzed the distribution of fluorescence intensities (FI) of F-actin and ZO-1 along the cell–cell junctions (detailed description in the Materials and Methods). Positive values represent with FI higher than the mean for the whole junction, and negative values indicate pixels with the FI lower than the average for the junction. The results of the junctional FI distributions in WT and KO cells with and without LatA treatments are visualized in violin plots (Fig. 7C,D). Untreated WT cells showed a 'drop-like' distribution, with most values around the mean FI (around zero), indicating equal protein distribution along the junction. LatA treatment of cells resulted in a spread of FI values, due to an increase of both strong positive and negative values. The number of negative values is significantly higher, as the localization of the proteins is limited to a few very intense spots. After the LatA washout (10 min and 60 min), FI values for F-actin and ZO-1 showed a stepwise recovery towards the FI distribution of

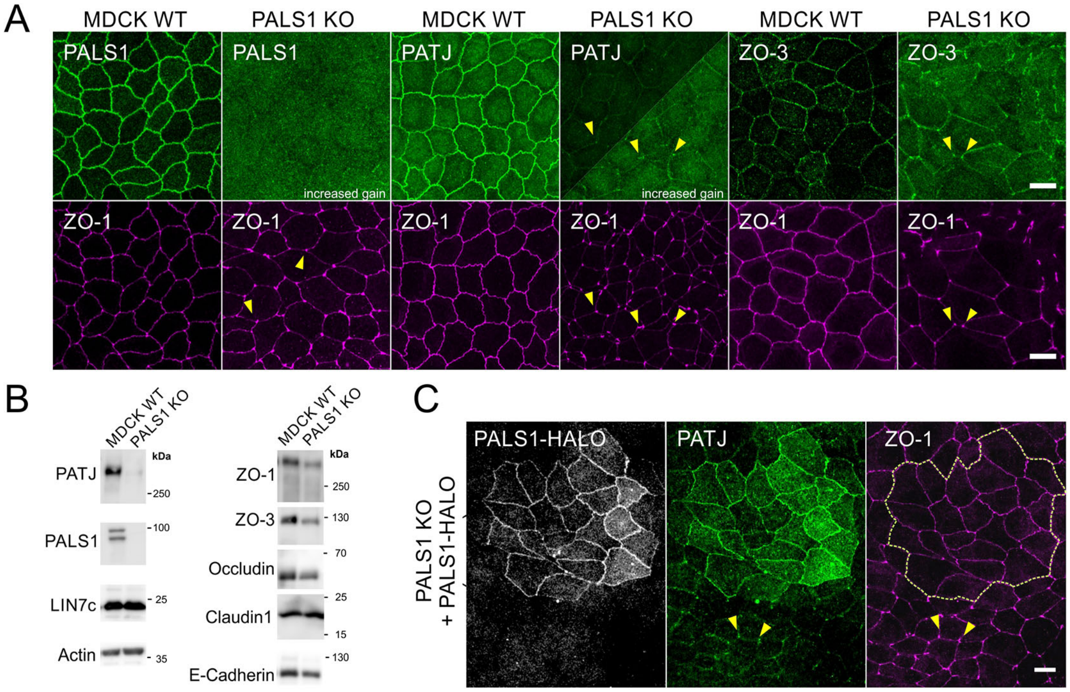

Fig. 4. PALS1 controls the lateral distribution of PATJ at cell junctions. (A) IF of WT and PALS1-KO cells. PALS1, PATJ and ZO-3 (green) showed colocalization with ZO-1 (magenta). In WT cells, these proteins show a chicken-wire-like distribution. In PALS1 KO cells, the signal intensity of PATJ, ZO-1 and ZO-3 is strongly reduced in along bicellular junctions (strongest reduction was observed for PATJ) accompanied by an enhanced signal intensity in tricellular junctions, resulting in dot-like distribution patterns. Scale bars: 10 µm. (B) Western blot analyses. WT and KO cells were analyzed for the expression of polarity proteins PALS1, PATJ, LIN7c and the junction proteins ZO-1, ZO-3, claudin 1 and E-cadherin. Actin served as loading control. PALS1 KO cells showed a very low expression level of PATJ and slightly reduced expression of TJ proteins ZO-1 and ZO-3. (C) IF studies of PALS1 KO cells expressing a PALS1–HALO fusion protein (rescue). Patches expressing the PALS1–HALO in PALS1 KO cells show targeting of PALS1–HALO fusion proteins to TJs (left). Expression of the PALS1–HALO fusion proteins re-established the expression and TJ associated localization of endogenous PATJ (middle panel) as well and the continuous distribution of ZO-1 (magenta). The yellow line marks rescue cells with PALS1–HALO expression. Scale bar: 10 µm. Yellow arrowheads in A and C highlight tricellular signal accumulation of PATJ or ZO-1 in PALS1 KO cells. Images representative of *n*=4 experiments.

untreated WT cells. The F-actin FI distributions of PALS1 KO cells resembled that of the WT cells, resulting in similar violin plot patterns. However, actin reassembly might be slightly delayed as after 10 min of washout as there was no stepwise rearrangement in the KO cells as seen in the WT (Fig. 7C,D). In contrast to F-actin recovery, LatA washout in PALS1 KO cells did not lead to recovery of the ZO-1 distribution (Fig. 7B,D). Together, these results demonstrate that PALS1 KO cells exhibit a strong defect in the reformation of TJs upon release from actin depolymerization.

In addition to the LatA washout experiments, we also conducted Ca^{2+} switch assays and analyzed the intracellular localization of ZO-1 and F-actin by IF analyses. The withdrawal of Ca^{2+} for 18 h resulted in a complete disassembly of TJs in WT and KO cells (Fig. 8). Both WT and KO cells showed a disrupted ZO-1 pattern accompanied by a ring-like F-actin distribution inside the cells (Fig. 8A,B). In WT cells, the re-establishment of F-actin belts and the uniform lateral distribution of TJ proteins along the bicellular and tricellular TJs occurred within 6 h of Ca^{2+} re-addition. By contrast, in PALS1 KO cells, the re-addition of Ca^{2+} only re-established the F-actin belt, whereas the distribution of ZO-1 remained incomplete, even after 24 h (Fig. 8B). In both junction reformation assays, we had the impression that the re-polymerization of F-actin in PALS1-depleted cells showed a slight delay. Since local actin polymerization can be regulated by the GTPase RhoA (de Seze et al., 2023; Terry et al., 2011), we analyzed the localization of RhoA in MDCK WT and PALS1 KO cells. Indeed, IF analyses of co-cultures demonstrated elevated levels of RhoA at the junctions formed between WT cells, with minimal RhoA signal detected in the cytosol. In contrast, KO cells exhibited reduced RhoA pools at cell–cell contacts (Fig. 8C).

DISCUSSION

In this study, we analyzed the functions of PALS1 in MDCK cells. Genetic inactivation of the *PALS1* gene using CRISPR/Cas9 resulted in an increased formation of multiple- and no-lumen cysts in 3D cell culture, and a strong increase in paracellular permeability in cysts derived from PALS1 KO cells. PALS1 KO cells that formed single-lumen cysts also showed an increase in paracellular permeability, whereas single- and multiple-lumen cysts of MDCK WT cells maintained a tight paracellular diffusion barrier for solutes at least up to 10 kDa. This is in line with earlier studies (Straight et al., 2004) and suggests that PALS1 is involved in the regulation of the paracellular transport of ions and solutes in epithelial cells and that the formation and function of TJs is not directly coupled to the establishment of a single apical luminal domain.

Proteins of the ZO family are essential for the formation of TJs and the regulation of paracellular transport in epithelia (Haas et al., 2022; Otani and Furuse, 2020; Otani et al., 2019; Umeda et al., 2006; Van Itallie et al., 2009; Zihni et al., 2016). Indeed, the loss of ZO-1 and ZO-2 in 3D MDCK cysts is associated with a dramatic increase in paracellular permeability to water, solutes and ions (Otani et al., 2019), and ZO-1/ZO-2 double KO cell lines show a phenotype similar to MDCK cells lacking PALS1 or the PALS1-binding site in PATJ (ΔL27-PATJ; (Pombo-García et al., 2022 preprint). PALS1-deficient cells revealed a significant reduction in TJ proteins along bicellular junctions, accompanied by an accumulation of

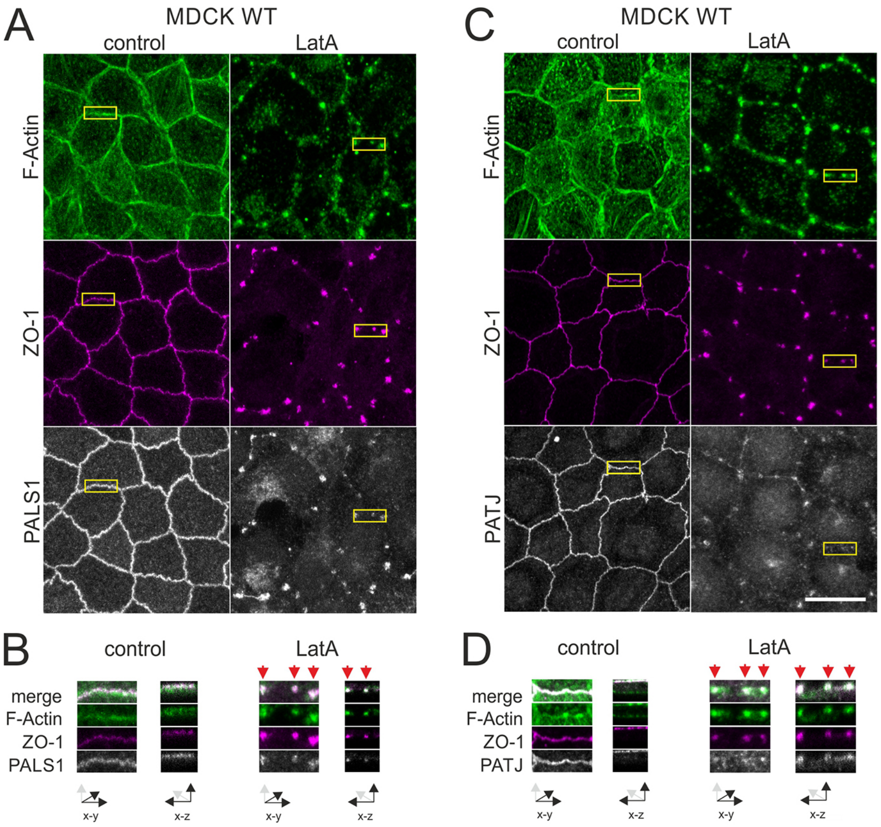

Fig. 5. Actin depolymerization results in dot-like distributions of PALS1 and PATJ along junctions. (A,C) IF of WT cells treated with LatA. F-actin depolymerization upon LatA treatment for 4 h leads to irregular F-actin (phalloidin-positive) accumulation inside the cytosol of cells and a dot-like pattern along the bicellular contacts. Junctional F-actin-positive dots (green) are also positive for ZO-1 and PALS1 (A) and PATJ (C). Scale bars: 10 µm. (B,D) Details of the IF studies (areas marked with yellow boxes in A and C) reveal that colocalization of F-actin and PALS1 or PATJ with the TJ protein ZO-1 is not only found in the *x-y* but also in *x-z* direction. Detailed views of the dot-like agglomerates (red arrows) underscore that there is colocalization in both dimensions as result of LatA treatment. Images representative of *n*=3 experiments.

these proteins at tricellular junctions, resulting in a dot-like (or spike-like) distribution pattern. Remarkably, this discontinuous distribution was preserved in bi- and tri-cellular junctions that were formed between WT and PALS1 KO cells. In other words, PALS1 KO cells that formed cell–cell contacts with cells that expressed PALS1 (MDCK WT cells) maintained a disrupted TJ distribution, indicating

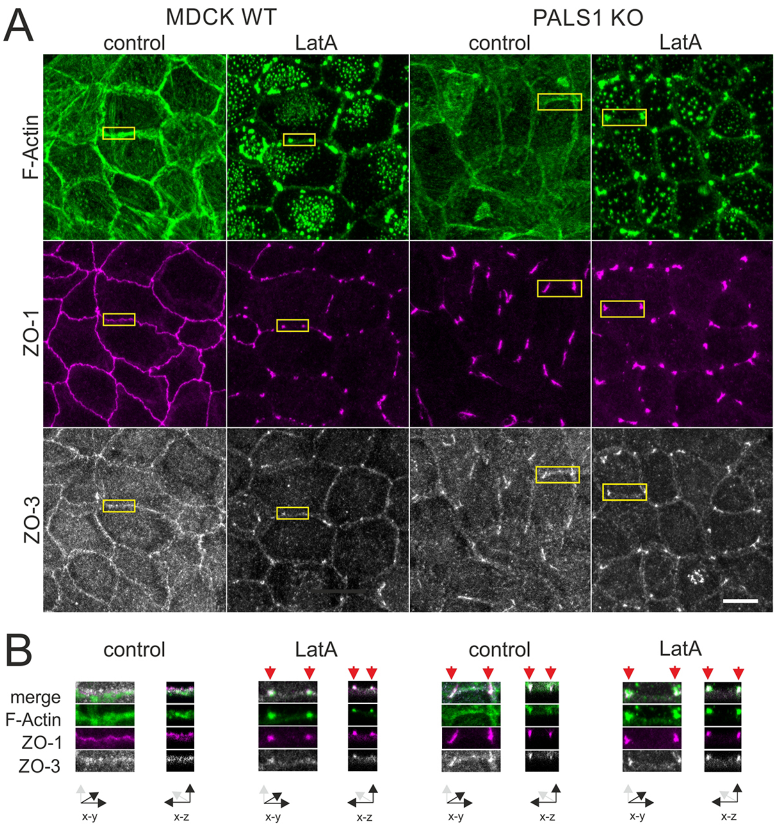

Fig. 6. Actin depolymerization and PALS1 depletion cause similar phenotypes. (A) IF of WT and PALS1 KO cells treated with LatA. Cells were stained with phalloidin (to visualize F-actin) and antibodies against ZO-1 and ZO-3. In comparison to untreated cells (control), F-actin depolymerization by LatA for 4 h leads to a dot-like F-actin pattern along the bicellular TJs and irregular F-actin accumulation inside the cytosol. Note that untreated PALS1 KO cells show a similar phenotype to LatA-treated WT cells. In WT and KO cells, junctional F-actin-positive dots (green) were also positive for ZO-1 (magenta) and ZO-3 (white). Scale bars: 10 µm. (B) Details of the IF studies (areas marked with yellow boxes in A) reveal that colocalization of F-actin with TJ proteins ZO-1 and ZO-3 (red arrows) is not only found in the *x-y* but also in the *x-z* direction in WT and PALS1 KO cells. Images representative of *n*=3 experiments.

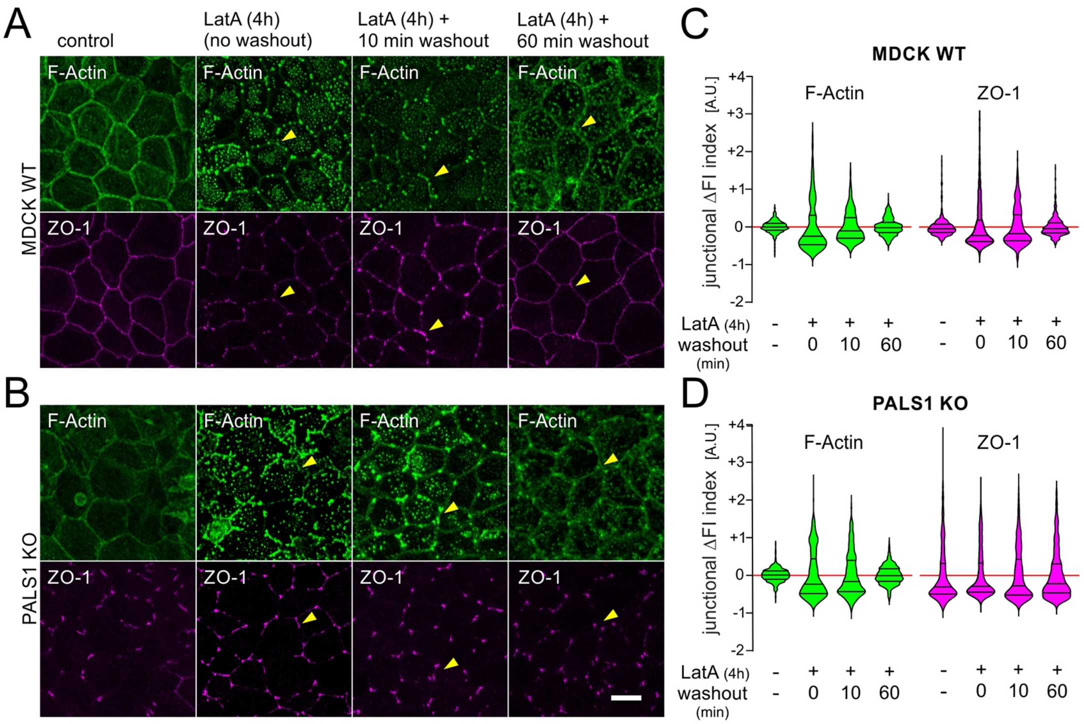

Fig. 7. Lateral elongation of TJ protein condensates via F-actin polymerization requires PALS1. (A–D) IF studies to evaluate the distribution of F-actin (green) and ZO-1 (magenta) along cell junctions of WT (A) and PALS1 KO cells (B) in the presence and absence of LatA. (A) IF analyses of F-actin and ZO-1 of WT cells treated with LatA (for 4 h) with or without subsequent washout of the LatA toxin after 10 min or 60 min. Untreated cells served as controls. In WT cells, withdrawal of LatA results in a complete re-establishment of the chicken-wire-like pattern of both F-actin and ZO-1 within 60 min. Yellow arrowheads highlight tricelluar junctions. (C) Violin plots summarizing changes in fluorescence intensity (FI) along bicellular junctions shown in A. Details concerning the 'junctional ΔFI index' are given in the Materials and Methods. (B) IF analyses of F-actin and ZO-1 of PALS1 KO cells treated with LatA (for 4 h) with or without subsequent LatA washouts after 10 min or 60 min. Untreated PALS1 KO cells served as controls. In PALS1 KO cells LatA-dependent depolymerization of F-actin is restored within 60 min, whereas the ZO-1 pattern kept its dot-like distribution. (D) Violin plots summarizing FI changes along bicellular junction shown in C. The data indicates that PALS1 (perhaps in concert with PATJ) is required to couple a F-actin polymerization-dependent elongation of ZO-1-positive condensates. Details of the evaluation are given in the Materials and Methods. Scale bars: 10 µm (*N*=3, total number of junctions *n*=12). Violin plots have the median and quartile boundaries marked.

that PALS1 on one side of cell–cell contacts is unable to trigger full TJ formation in adjoining cells. These data collectively suggest two things: first, PALS1 governs the correct lateral distribution of TJ proteins along bicellular contacts and, second, the continuous lateral distribution of ZO-1 at intercellular TJs is directly associated with the cell autonomous expression of PALS1.

PALS1 binds to PATJ, which in turn binds to the TJ proteins ZO-3 and claudin 1, via the sixth and eighth PDZ domain, respectively (Roh et al., 2002b). Moreover, previous studies identified the L27N domain of PALS1 as the PATJ-binding module that targets PALS1 to TJs, demonstrating that membrane targeting of PALS1 requires the presence of PATJ (Roh et al., 2002a) and suggesting that PALS1 localization requires PATJ.

We show here that PALS1, in turn, controls the protein level and the localization of PATJ to bicellular TJs, because in PALS1 KO and KD cells PATJ expression was strongly reduced and residual PATJ was no longer efficiently targeted to bicellular TJs. Several other TJ proteins were similarly affected.

Moreover, PALS1 deletion mutants lacking the L27N domain did not rescue the ZO-1 distribution phenotype of PALS1 KO cell lines. These PALS1 KO phenotypes, together with previous work showing that PATJ regulates the localization of occludin and ZO-3 to TJs (Michel et al., 2005), argue for a tight functional symbiosis between PALS1 and PATJ, in which PALS1 likely acts as a stabilizing factor upstream of PATJ to trigger the continuous distribution of TJ proteins. Recent super-resolution imaging studies demonstrating a high degree of co-localization of these proteins at the apical-lateral border support the strong interconnection between PALS1 and PATJ (Mangeol et al., 2022).

Recently, it has been demonstrated that phase separation of ZO proteins drives the formation of TJs (Beutel et al., 2019; Schwayer et al., 2019). Strikingly, cells lacking PATJ, or expressing a PATJ variant lacking the PALS1-binding module (ΔL27-PATJ) failed to form a continuous TJ belt due to reduced spreading dynamics of ZO-1 condensates (Fiedler et al., 2023; Pombo-García et al., 2022 preprint). Intriguingly, the disrupted ZO-1 distribution along bicellular junctions in ΔL27-PATJ MDCK cells strongly resembles the dot-like pattern that we observed in MDCK PALS1 KO and KD cell lines (Pombo-García et al., 2022 preprint). These observations strengthen the hypothesis that the close functional coupling between PALS1 and PATJ is required for the formation of a continuous and functional TJ belt in epithelial cells. Therefore, our observations along with those by Pombo-Garcia et al., and earlier studies by the groups of Margolis and Le Bivic indicate that the lateral continuous belt formation of ZO-1 (and other TJ proteins) might be predominantly organized via a PALS1–PATJ axis (Michel et al., 2005; Pombo-García et al., 2022 preprint; Roh et al., 2002a; Straight et al., 2004).

Moreover, F-actin polymerization and actomyosin-mediated contractility are known to control TJ formation and epithelial permeability (Belardi et al., 2020; Ivanov et al., 2005; Van Itallie et al., 2009, 2015). Depolymerization of the F-actin cytoskeleton results in disrupted TJs in which the colocalization of F-actin and TJ

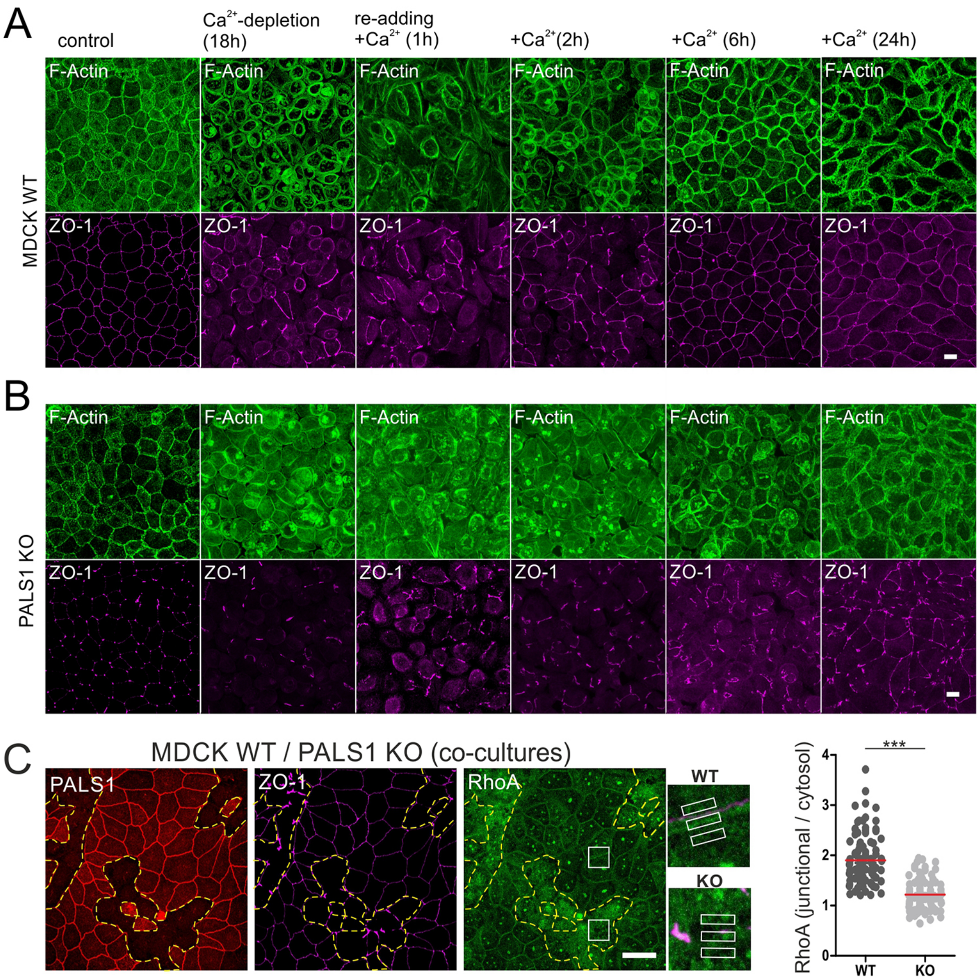

Fig. 8. PALS1 KO show cells a delayed TJ formation. (A,B) IF of WT (A) and PALS1 KO cells (B) in Ca^{2+} switch experiments. F-actin was stained by phalloidin; antibody staining against ZO-1 served as a TJ marker. Depletion of Ca^{2+} leads to a complete disassembly of TJs and disordered F-actin signal in WT and PALS1 KO cells. Refeed with medium containing Ca^{2+} results in a stepwise reassembly of the F-actin belt and continuous distribution of ZO-1 at the TJs after 6 h in WT cells. In PALS1 KO cells, the F-actin belt could be restored after re-addition of Ca^{2+}; however, the TJ marker ZO-1 remained discontinuously distributed, even after 24 h of Ca^{2+} refeed. Scale bars: 10 µm. Images in A and B are representative of *n*=3 experiments. (C) IF of WT and PALS1 KO co-cultures stained for RhoA. Co-staining of PALS1 was used to identify KO cells and ZO-1 staining was used as a TJ marker. In both WT and KO cells, RhoA was localized at the junction. However, PALS1 KO cells additionally showed a diffuse and stronger cytosolic signal. For quantifying the subcellular RhoA distribution, the FI at the junction was normalized to that of the cytosol of both surrounding cells (selected areas shown in detailed images). PALS1 KO resulted in a significant decrease of the ratio (junctional FI/cytosol FI), indicating an alteration of the subcellular RhoA localization (*N*=4, total *n*=100). ***$P<0.001$; Mann–Whitney U-test).

proteins is maintained (Stevenson and Begg, 1994; Sun et al., 2023 preprint). Recently, the groups led by Honigmann and Weber suggested that receptor-mediated clustering of ZO-1 is coupled to actin polymerization and bundling, which drives elongation of ZO-1 along the TJ (Sun et al., 2023 preprint). According to the proposed model, actin polymerization is the rate-limiting process for TJ belt elongation (Sun et al., 2023 preprint). Our current data indicate that the situation might be more complicated, as polymerization of actin in the absence of PALS1 is not able efficiently drive TJ elongation. In contrast to the biochemical *in vitro* experiments by Sun and colleagues, where weak binding of ZO-1 to actin via the actin binding regions (ARBs) was sufficient to accelerate actin polymerization and couple ZO-1 elongation along F-actin fibers, in MDCK cells this ZO-1–actin coupling requires PALS1 (this study) and most likely other members of the CRB complex (Pombo-García et al., 2022 preprint). Taken together, this suggests that TJ formation relies on two interconnected self-assembly processes: on the one hand, localized actin polarization along TJ (Sun et al., 2023 preprint), and, on the other hand, a phase separation-dependent condensation of cytoplasmic TJ proteins (such as ZO proteins) followed by elongation along bicellular TJs (Beutel et al., 2019; Schwayer et al., 2019). Our findings underscore a role for PALS1 – and likely PATJ – in the spatiotemporal coordination of these processes, which is essential for the lateral elongation of TJ protein condensates.

Interestingly, we observed decreased RhoA pools at TJs in PALS1 KO cells. Although it remains unknown to what extent these RhoA pools are activated, it is tempting to speculate that reduced RhoA pools in PALS1-depleted cells might correlate with diminished local RhoA-dependent F-actin polymerizations. It has been demonstrated previously that PATJ binds to and recruits p114RhoGEF (also known as ARHGEF18) to apical cell junctions of epithelial cells (Nakajima and Tanoue, 2011, 2012). Interestingly, this interaction appears to be conserved, as the RhoGEF Cysts, a *Drosophila* ortholog of p114RhoGEF, is also recruited to junctional membranes through an interaction with the *Drosophila* CRB complex (Silver et al., 2019). Moreover, p114RhoGEF activates local RhoA pools at TJs and thereby plays a crucial role in the formation of the circumferential F-actin belt (Terry et al., 2011). Strikingly, depletion of p114RhoGEF in MDCK cells caused a similar phenotype to that seen in MDCK cells lacking PALS1, with disrupted TJs and multiple lumen formation in 3D cultures (Terry et al., 2011). This together with our data provides evidence that a PALS1–PATJ–p114RhoGEF–RhoA axis regulates the F-actin-dependent formation of TJ in epithelia.

However, the situation is probably far more complex, as most TJ and polarity proteins are large multi-domain scaffolding proteins with numerous protein–protein interaction domains (Fanning and Anderson, 2009; Martin et al., 2021; Otani and Furuse, 2020; Rouaud et al., 2020; Thompson et al., 2013). PATJ, for example, contains up to 10 PDZ domains that mediate interactions with other proteins, including TJ proteins and several components of the Hippo signaling pathway (Duning et al., 2008, 2010; Ernkvist et al., 2009; Kohli et al., 2014; Morthorst et al., 2022; Roh et al., 2002b; Varelas et al., 2010; Wells et al., 2006). Of note, recent proximity labeling studies have identified additional binding partners of PATJ (e.g. HOMER proteins) that might provide links to TJ proteins, regulate F-actin formation or dynamics at TJ or control epithelial functions beyond the formation of cell–cell contacts (Tan et al., 2020). Finally, there is evidence that not only F-actin but also other components of the cytoskeleton, such as microtubules or members of the septin protein family control TJ formation in epithelial cells (Bowen et al., 2011; Yano et al., 2021). Given that p114RhoGEF has also been identified as a septin-associated GEF (Nagata and Inagaki, 2005) it is possible that mechanisms other than RhoA-mediated F-actin dynamics contribute to the PALS1 KO phenotypes we present here.

The epithelia of the nephron segments in the kidney ensure the excretion of noxious substances and the concentration of the primary ultra-filtrate into the final urine, as well as the recycling and resorption of numerous nutrients, organic and inorganic ions. In other words, minor changes in TJ formation dynamics, maintenance or in the distribution of central TJ proteins might have very severe consequences *in vivo*. The dysfunctional lateral distribution of TJ proteins in PALS1 KO and KD cells and the strong phenotype of Pals1 haplo-insufficient mice in which even a partial Pals1 depletion causes severe defects – although the well-defined apicobasal distribution of important proteins is in principle preserved – supports this assumption (Berghaus et al., 2022; Weide et al., 2017). Further research will be necessary to clarify to what extent even minor modifications of the ‘tightness of TJs’ contribute to pathomechanisms and how the complex interplay between polarity, junction assembly and cytoskeleton modulation is regulated.

MATERIALS AND METHODS

Constructs and cloning

We generated pENTR constructs with human PALS1 cDNA inserts (Gene ID: 64398) encoding for PALS1 full length (aa 1–675) and two PALS1 deletion mutants (ΔECR, aa 118–674; ΔL27N, aa 178–675) using the pENTR^{TM} Directional TOPO® Cloning Kit (Invitrogen). The pENTR constructs were shuttled into modified pQCXIH-GW-GFP or pQCXIH-GW-Halo plasmids using the L/R reaction of the Gateway^{TM} Cloning system (Invitrogen), according to the manufacturer’s instructions. All primers and oligonucleotides are listed in Table S1.

Generation and establishment of PALS1 knockout cell lines

To generate a PALS1 knockout in MDCKII cells (Sigma, #ECACC 00062107) frameshift mutations were introduced via CRISPR/Cas9. CRISPOR (Concordet and Haeussler, 2018) was used to design the following guide RNA/DNA-sequences 5′-CACCGATCATTAGTCGGATAGTAAA-3′ and 5′-AAACTTTACTATCCGACTAATGATC-3′. The gRNAs (100 µM, 8 µl each) were phosphorylated and annealed via adding 2 µl 10× PNK buffer, 1 µl ATP (5 mM) and 1 µl polynucleotide kinase (Promega, M4101) and incubation for 1 h at 37°C followed by incubation at 95°C for 5 min to stop the reaction. Resulting oligonucleotides were inserted into the px459 plasmid via digestion using BbsI and ligation by T4 ligase (Thermo Fisher Scientific, EL0011). pSpCas9(BB)-2A-Puro (PX459) V2.0 was Addgene plasmid #62988 (deposited by Feng Zhang; Ran et al., 2013). MDCK cells with a confluency of 60% were transfected using Lipofectamine™ 2000 following the manufacturer’s protocol. Selection was done using puromycin (4 µg/ml, Invivogen, ant-pr) for 48 h. Potential knockout cells were separated to analyze single cell clones. Potential clones were sequenced and only clones with frameshift mutations were kept. Heterozygous clones were further analyzed after cloning with Zero Blunt® TOPO® PCR cloning kit to separate individual alleles.

Cultivation of MDCK II cell lines

MDCK WT (Merck/Sigma, ECACC 00062107) and PALS1 KO (MDCK WT cells with CRISPR/Cas9-mediated knockout of the *PALS1* gene) cell lines were grown in modified Eagle’s medium (MEM, Lonza) containing 5% fetal calf serum (FCS; Bio&Sell, FBS.S 0615) and 1% 100× penicillin/streptomycin/l-glutamine (P/S/G; Sigma, G6784). HEK293T cells were grown in DMEM medium containing 10% FCS and 1% P/S/G. The cells were cultivated at 37°C and 5% CO_2. For transient transfection, cells were transfected using Lipofectamine™ 2000 according to the manufacturer’s manual.

MDCK cells were seeded on coverslips, on ThinCert™ cell culture inserts (0.4 mm-pore transwell filters, Greiner Bio-one) to reach full polarization, or in a matrix hydrogel (basement membrane extract, BME, from R&D Systems) in three dimensions (3D) to form cysts. Medium was exchanged every other day. On coverslips cells were grown up to a confluency of 100%, in transwell filters for 7–10 days and in BME for 5-7 days before using them for immunofluorescence staining. In case of mixed monolayers, wildtype and KO cells were mixed 1:1 and seeded on coverslips or ThinCert™ cell culture inserts, respectively.

Generation of stable cell lines

Stable cell lines were generated via retroviral gene transfer, as described previously (Schulze et al., 2014). In brief, HEK293 T cells were transiently transfected with the helper plasmids pCMV-VSV-G and pUMVC and pQCXIH plasmids encoding for full-length PALS1 or deletion mutants fused to HALO or EGFP fluorescence tags. Supernatant containing the virus particles were added to MDCK WT and PALS1 KO cells after being filtered through a sterile 0.45 µm filter (Millipore). Here, one volume of MEM including supplements was mixed with one volume of virus-containing medium supplemented with polybrene (8 µg/ml). After 24 h, virus-containing medium was collected and stored at 4°C. Cells were left in medium without virus to regenerate for 24 h. After regeneration period, the second round of transduction using the same virus-containing medium was performed for another 24 h. After another 24 h for regeneration, transduced cells were selected using hygromycin (250 µg/ml). All established cell lines were tested for a constitutive overexpression of PALS1 proteins by live-cell imaging or western blotting.

Generation of PALS1 shRNA lines

Short hairpin RNAs (shRNAs) were purchased as complementary oligonucleotides that when annealed contained the HindIII (5′) and BamHI (3′) sticky ends for cloning into the pSuper vector (Oligoengine). The PALS1 shRNA B oligonucleotides had the following sequence: 5′-CCGGAGATGAGGTTCTGGAAATTCAAGAGATTTCCAGAACCTCATCTCCTTTTT-3′ (underlining highlights the targeting sequence). All plasmids were verified by Sanger sequencing. The shRNA-transfected MDCK cells were grown in 200 µg/ml hygromycin to select for stable clonal cell lines. The PALS1 rescue line was generated by transfecting shRNA-resistant PALS1–GFP into the clonal PALS1 shRNA line B1, followed by clonal selection in 400 µg/ml geneticin (Tan et al., 2020). PALS1 shRNA and PALS1-GFP rescue IF and western blotting experiments were performed as described previously (Tan et al., 2020).

Junction assembly assay – LatA treatment and Ca^{2+} switch assay

For analyses of junction reformation in MDCK WT and PALS1 KO cells, Ca^{2+} detraction or LatA treatment were used. Prior to treatment, cells were grown on ThinCert™ cell culture inserts (12-mm, 0.4 mm-pore transwell filters, Greiner Bio-one) for 7 days. For Ca^{2+} switch experiments, cells were washed three times with 1× PBS and cultivated for 18 h in Ca^{2+} reduced medium (Sigma, M8167). For refeed of the cells, this Ca^{2+} depletion was followed by re-cultivation in normal cultivation medium (containing Ca^{2+}) for 1–24 h before cells were fixed and used for IF staining. For LatA experiments, cells were treated with 1 µM LatA (Sigma, L5163) for 4 h. Afterwards, washout was performed by replacing the medium with normal cultivation medium for 10 min, 60 min before cells were fixed and stained.

TEER measurements

MDCK cells were seeded on ThinCert™ cell culture inserts (12-mm, 0.4 mm-pore transwell filters, Greiner Bio-one) to measure the transepithelial electrical resistance (TEER). The electrical resistance between the apical and the basolateral chamber was measured using a two-electrode resistance system. To calculate the unit area resistance ($\Omega\times\text{cm}^2$), the electric resistance was multiplied by the growth area of the Transwell filters (1.13 cm^2). The TEER measurement was performed with an interval of 5 min from the moment of seeding the cells to 7 days after seeding. Medium was changed once after 3–4 days. Values were normalized to the WT control values.

For TEER measurement after Ca^{2+} depletion (Ca^{2+} switch assay) to break down the established junctions, cells were grown for 7 days on ThinCert™ cell culture inserts in cultivation medium until confluency. For Ca^{2+} reduction, cells were washed three times with 1× PBS and cultivated for 18 h in Ca^{2+} reduced medium (Sigma, M8167). Subsequently, Ca^{2+} reduced medium was replaced by normal cultivation medium (containing Ca^{2+}). TEER measurement was started immediately and performed every 5 min for 24 h. Values were normalized to a medium control (well without cells).

Generation of 3D cysts and permeability assay

To grow 3D MDCK cysts, ibidi µ-Slide 8-well chambers were coated with 8 µl BME [(Bio-Techne (R&D Systems), Cultrex PathClear ReducedGrowth Factor BME, Type 2; cat. no. 3533-005-02]. For solidification of the BME-coated, wells were incubated at 37°C with 5% CO_2 for 15–30 min. Cells were detached from a two-dimensional (2D) monolayer using incubation at 37°C with 5% CO_2 in 10× trypsin/EDTA solution until reaching a single-cell suspension. Cells were seeded (5000 cells/cm^2), resuspended in 250 µl in medium containing 10% FCS, 1% P/S/G and 2.5% BME. Cells were cultured for 5–7 days at 37°C with an atmospheric CO_2 concentration of 5%. Medium was exchanged every second day. Cysts were either used for immunofluorescence staining (7 days) or for 3D permeability assays (5 days).

To measure the permeability of cysts, fluorescently labeled dextran of different sizes was used (Alexa Fluor 647, 10 kDa; FITC, 3-5 kDa). Medium was exchanged with 200 µl live-cell imaging medium (15 mM HEPES in Hanks' balanced salt solution). Cysts were imaged live using the HC PL APO 40×/1.10 W motCORR CS2 objective of a confocal microscope (TCS SP8, Leica Biosystems). Cysts were imaged every minute for 15–20 min in total. The permeability assays were performed with simultaneous detection of both dextran samples: FITC-labeled 3–5 kDa dextran and Alexa Fluor 647-labeled 10 kDa dextran. After imaging time point t_0, medium was supplemented with 50 µl dextran solution (10 µM Alexa Fluor 647, 12.5 µM FITC). Cyst permeability was quantified by determining the signal intensity, comparing the lumen intensity against the average intensity outside of the cyst.

Transmission electron microscopy

MDCK cysts cultivated in cell culture plates were washed with PBS and then fixed in 2% (v/v) formaldehyde and 2.5% (v/v) glutaraldehyde in 100 mM cacodylate buffer, pH 7.4, at 4°C overnight. After washing in PBS, specimens were postfixed in 0.5% (v/v) osmium tetroxide and 1% (w/v) potassium hexacyanoferrate (III) in 0.1 M cacodylate buffer for 2 h at 4°C followed by washing with distilled water. After dehydration in an ascending ethanol series from 30% to 100% ethanol, specimens were two times incubated in propylene oxide each for 15 min. The cells were detached from the surface of the cell culture plate during the propylene oxide treatment. Finally, detached cells were embedded in Epon using Beem capsules. Ultrathin sections were cut on an ultramicrotome and collected on copper grids. Electron micrographs were taken at a Phillips EM-410 electron microscope using imaging plates (Ditabis, Pforzheim, Germany).

Preparation of cell lysates and western blot analyses

Cells were grown on six-well plates up to a confluency of 95%, washed twice with 1× PBS and lysed with 300 µl 1× SDS sample buffer [20% (v/v) glycerin, 125 mM Tris-HCl pH 6.8, 10% (w/v) SDS, 0.2% (w/v) Bromophenol Blue, 5% mercaptoethanol and 1 l H_2O]. For homogenization, samples were passed through a blunt 20 G needle (0.9 mm diameter) and heated up to 95°C. Lysates were centrifuged for 1 min at 14,000 ***g*** and stored at −20°C until usage.

Western blot analysis was performed as previously described (Berghaus et al., 2022; Weide et al., 2017). First, cell lysates were boiled at 95°C for 5 min. Proteins were separated via SDS-PAGE using 10% gels (Bio-Rad). Then, proteins were transferred to a PVDF membrane (Millipore) following by incubation in blocking powder (5% milk powder in TBST [0.05% Tween 20]) for 1 h at room temperature (RT). Probes were incubated with primary antibodies (Table S2) diluted in BSA (2.5 g BSA powder in 50 ml TBST) o/n at 4°C. Afterwards, the membrane was washed three times with TBST followed by incubation with horseradish peroxidase coupled secondary antibodies (Table S3) for 1 h at RT. The membrane was washed again for three times with TBST before a chemiluminescence detection reagent (Clarity; Bio-Rad) was added and the membrane was imaged using an Azure Biosystems imager (c600; Azure Biosystems). Uncropped images of western blots are shown in Fig. S8.

Immunofluorescence analysis

Cells on coverslips and Transwell filter insets were grown either as pure cultures or as co-cultures of two different cell lines mixed in a ratio of 1:1. 3D cysts were grown as described above. All cells were washed twice with cold 1× PBS and fixed in 4% paraformaldehyde (PFA) for 20 min at RT. After cells were washed three times with 1× PBS, they were quenched for 10 min in 50 mM NH_4Cl followed by another three rounds of washing in 1× PBS. Then, cells were permeabilized in 0.2% Triton X-100 for 5 min. After washing the cells three times in IF wash buffer [0.2% (w/v) gelatin, 10% (v/v) 10× PBS, 0.2% (v/v) Triton X-100 and H_2O)] and blocked [90% (v/v) IF wash buffer, 10% (v/v) normal goat serum (NGS) for 20 min at RT. Cells were incubated o/n in antibody dilutions buffer (98% (v/v) IF wash buffer 2% (v/v) NGS, containing specific antibodies (Table S2). Next, cells were washed three times with IF wash buffer and transferred into fluorophore-conjugated secondary antibodies (Table S3) solved in antibody solution containing DAPI (1:5000). After an incubation of 30 min at RT, cells were washed the last time with 1× PBS and were carefully rinsed in distilled H_2O before either being mounted in 6–12 µl mowiol on object slides (coverslips, ThinCert™ cell culture inserts) or in IMM mounting medium (ibidi GmbH, Cysts). Samples were imaged on a confocal microscope (TCS SP8, Leica Biosystems) using a 40× water objective or a spinning disk microscope (CorrSight, Thermofisher) using a 40× or 63× oil objective (NA 1.3 or 1.4; Zeiss Plan Apochromat). Confocal stacks were processed, and analyses were performed with Fiji. Final figures were mounted using CorelDRAW.

Image analyses

Images were analyzed with Fiji (https://fiji.sc/). Movies were created using LAS X (Leica Biosystems). For quantification of the RhoA level, co-cultures of MDCK WT and PALS1 KO cells grown on ThinCert™ cell culture inserts were stained for RhoA, ZO-1 and PALS1 as described before and imaged via confocal microscopy. Fluorescence intensity (FI) measurements were performed in Fiji using maximum intensity projection images of the confocal stacks. Localization of RhoA was measured as RhoA FI at the TJ region (apicobasal plane defined by ZO-1) of a cell–cell contact compared to the cytoplasmic FI within the two neighboring cells building the contact. RhoA FI was analyzed in cell–cell contacts in corresponding WT–WT or KO–KO cells and, for quantification, the intensities at the junction were normalized to the values of the corresponding cytosols.

For analyzing of the distribution of F-actin and ZO-1 along the TJ region, violin plot profiles of the bicellular junction were created. Resulting FIs for each pixel were normalized to the mean FI of each junction. To determine the deviation from an equal protein distribution along the junction (relative fluorescence=1) each normalized value had 1 subtracted. Results of this analysis were visualized as violin plots. Hence, values >0 are equal to increased FI per pixel, whereas values <0 visualize pixels with reduced FI values compared to an equal fluorescence signal at the junction (junctional ΔFI Index). The effect of LatA treatment was visualized by examining the *xy* distribution of proteins along the junction using the maximum projection images. The apical-basal distribution of junction proteins was shown by examining the *xz* images resulting from *z*-stacks.

Quantification and statistical evaluation

Each experiment was performed at least n=3 times. Graphs were created and statistical analysis was performed with the GraphPad PRISM software. Data show the mean±s.e.m. The value of n and the definition is indicated in the corresponding figure legends and results. For comparison of two groups, the Mann–Whitney U test was used, for comparison of more than two groups the Kruskal–Wallis-test was performed corrected for multiple testing with the Dunn's correction. *$P<0.05$, **$P<0.01$, ***$P<0.001$. If not indicated differently, all data represent at least three independent repeats.

Acknowledgements

We would like to thank Dr Alf Honigmann (MPI Dresden) for providing us details of the permeability protocol. We would like to thank Karin Gäher for excellent technical support.

Competing interests

The authors declare no competing or financial interests.

Author contributions

Conceptualization: P.N., M.P.K., K.E., H.P., A.L., T.W.; Methodology: A.-C.G., A.M.-K., K.G., V.H., P.N., S.K., M.B., S.G., U.H.; Software: K.G.; Validation: A.-C.G., A.M.-K., K.G., V.H., P.N., S.K., M.B., S.G., U.H., A.L., T.W.; Formal analysis: A.-C.G., A.M.-K., K.G., V.H., P.N., S.K., M.B., S.G., U.H., M.P.K., K.E., H.P., A.L., T.W.; Investigation: A.-C.G., A.M.-K., K.G., V.H., S.K., M.B., S.G., U.H.; Data curation: A.L., T.W.; Writing - original draft: A.-C.G., T.W.; Writing - review & editing: P.N., K.E., H.P., A.L., T.W.; Visualization: A.-C.G., T.W.; Supervision: T.W.; Project administration: T.W.; Funding acquisition: A.L., T.W.

Funding

The work was supported by Deutsche Forschungsgemeinschaft (DFG) grant (WE 2550/4-1 of SPP1782 and WE 2550/5-1) to T.W. and by the Graduate School of the Cells-in-Motion Cluster of Excellence (EXC 1003 – CiM to A.-C.G.). This research was supported by the Ministry of Education, Singapore, under its Academic Research Fund Tier2 (MOE-T2EP30121-0019) to A.L.

Data availability

The data and tools that support the findings of this study are available from the corresponding author upon reasonable request.

Peer review history

The peer review history is available online at https://journals.biologists.com/jcs/lookup/doi/10.1242/jcs.261303.reviewer-comments.pdf.

References

Belardi, B., Hamkins-Indik, T., Harris, A. R., Kim, J., Xu, K. and Fletcher, D. A. (2020). A weak link with actin organizes tight junctions to control epithelial permeability. *Dev. Cell* **54**, 792-804.e7. doi:10.1016/j.devcel.2020.07.022

Berghaus, C., Groh, A. C., Breljak, D., Ciarimboli, G., Sabolić, I., Pavenstädt, H. and Weide, T. (2022). Impact of Pals1 on expression and localization of transporters belonging to the solute carrier family. *Front. Mol. Biosci.* **9**, 792829. doi:10.3389/fmolb.2022.792829

Beutel, O., Maraspini, R., Pombo-García, K., Martin-Lemaitre, C. and Honigmann, A. (2019). Phase separation of zonula occludens proteins drives formation of tight junctions. *Cell* **179**, 923-936.e11. doi:10.1016/j.cell.2019.10.011

Bowen, J. R., Hwang, D., Bai, X., Roy, D. and Spiliotis, E. T. (2011). Septin GTPases spatially guide microtubule organization and plus end dynamics in polarizing epithelia. *J. Cell Biol.* **194**, 187-197. doi:10.1083/jcb.201102076

Charrier, L. E., Loie, E. and Laprise, P. (2015). Mouse Crumbs3 sustains epithelial tissue morphogenesis in vivo. *Sci. Rep.* **5**, 17699. doi:10.1038/srep17699

Concordet, J.-P. and Haeussler, M. (2018). CRISPOR: intuitive guide selection for CRISPR/Cas9 genome editing experiments and screens. *Nucleic Acids Res.* **46**, W242-W245. doi:10.1093/nar/gky354

De Seze, J., Gatin, J. and Coppey, M. (2023). RhoA regulation in space and time. *FEBS Lett.* **597**, 836-849. doi:10.1002/1873-3468.14578

Duning, K., Schurek, E.-M., Schlüter, M., Bayer, M., Reinhardt, H.-C., Schwab, A., Schaefer, L., Benzing, T., Schermer, B., Saleem, M. A. et al. (2008). KIBRA modulates directional migration of podocytes. *J. Am. Soc. Nephrol.* **19**, 1891-1903. doi:10.1681/ASN.2007080916

Duning, K., Rosenbusch, D., Schlüter, M. A., Tian, Y., Kunzelmann, K., Meyer, N., Schulze, U., Markoff, A., Pavenstädt, H. and Weide, T. (2010). Polycystin-2 activity is controlled by transcriptional coactivator with PDZ binding motif and PALS1-associated tight junction protein. *J. Biol. Chem.* **285**, 33584-33588. doi:10.1074/jbc.C110.146381

Elia, N. and Lippincott-Schwartz, J. (2009). Culturing MDCK cells in three dimensions for analyzing intracellular dynamics. *Curr. Protoc. Cell Biol.* **43**, 4.22.1-4.22.18. doi:10.1002/0471143030.cb0422s43

Ernkvist, M., Persson, N. L., Audebert, S., Lecine, P., Sinha, I., Liu, M., Schlueter, M., Horowitz, A., Aase, K., Weide, T. et al. (2009). The Amot/Patj/Syx signaling complex spatially controls RhoA GTPase activity in migrating endothelial cells. *Blood* **113**, 242-253. doi:10.1182/blood-2008-04-153874

Fanning, A. S. and Anderson, J. M. (2009). Zonula occludens-1 and −2 are cytosolic scaffolds that regulate the assembly of cellular junctions. *Ann. N. Y. Acad. Sci.* **1165**, 113-120. doi:10.1111/j.1749-6632.2009.04440.x

Fanning, A. S., Ma, T. Y. and Anderson, J. M. (2002). Isolation and functional characterization of the actin binding region in the tight junction protein ZO-1. *FASEB J.* **16**, 1835-1837. doi:10.1096/fj.02-0121fje

Fiedler, J., Moennig, T., Hinrichs, J. H., Weber, A., Wagner, T., Hemmer, T., Schröter, R., Weide, T., Epting, D., Bergmann, C. et al. (2023). PATJ inhibits histone deacetylase 7 to control tight junction formation and cell polarity. *Cell. Mol. Life Sci.* **80**, 333. doi:10.1007/s00018-023-04994-3

Fogg, V. C., Liu, C. J. and Margolis, B. (2005). Multiple regions of Crumbs3 are required for tight junction formation in MCF10A cells. *J. Cell Sci.* **118**, 2859-2869. doi:10.1242/jcs.02412

Haas, A. J., Zihni, C., Krug, S. M., Maraspini, R., Otani, T., Furuse, M., Honigmann, A., Balda, M. S. and Matter, K. (2022). ZO-1 guides tight junction assembly and epithelial morphogenesis via cytoskeletal tension-dependent and -independent functions. *Cells* **11**, 3775. doi:10.3390/cells11233775

Hurd, T. W., Gao, L., Roh, M. H., Macara, I. G. and Margolis, B. (2003). Direct interaction of two polarity complexes implicated in epithelial tight junction assembly. *Nat. Cell Biol.* **5**, 137-142. doi:10.1038/ncb923

Iden, S., Misselwitz, S., Peddibhotla, S. S. D., Tuncay, H., Rehder, D., Gerke, V., Robenek, H., Suzuki, A. and Ebnet, K. (2012). aPKC phosphorylates JAM-A at Ser285 to promote cell contact maturation and tight junction formation. *J. Cell Biol.* **196**, 623-639. doi:10.1083/jcb.201104143

Ivanov, A. I., Hunt, D., Utech, M., Nusrat, A. and Parkos, C. A. (2005). Differential roles for actin polymerization and a myosin II motor in assembly of the epithelial apical junctional complex. *Mol. Biol. Cell* **16**, 2636-2650. doi:10.1091/mbc.e05-01-0043

Kohli, P., Bartram, M. P., Habbig, S., Pahmeyer, C., Lamkemeyer, T., Benzing, T., Schermer, B. and Rinschen, M. M. (2014). Label-free quantitative proteomic analysis of the YAP/TAZ interactome. *Am. J. Physiol. - Cell Physiol.* **306**, C805-C818. doi:10.1152/ajpcell.00339.2013

Lemmers, C., Michel, D., Lane-Guermonprez, L., Delgrossi, M. H., Médina, E., Arsanto, J. P. and Le Bivic, A. (2004). CRB3 binds directly to Par6 and regulates the morphogenesis of the tight junctions in mammalian epithelial cells. *Mol. Biol. Cell.* **15**, 1324-1333. doi:10.1091/mbc.e03-04-0235

Mangeol, P., Massey-Harroche, D., Richard, F., Concordet, J.-P., Lenne, P.-F. and Le Bivic, A. (2022). Super-resolution imaging uncovers the nanoscopic segregation of polarity proteins in epithelia. *Elife* **11**, e62087. doi:10.7554/eLife.62087

Martìn-Padura, I., Lostaglio, S., Schneemann, M., Williams, L., Romano, M., Fruscella, P., Panzeri, C., Stoppacciaro, A., Ruco, L., Villa, A. et al. (1998). Junctional adhesion molecule, a novel member of the immunoglobulin superfamily that distributes at intercellular junctions and modulates monocyte transmigration. *J. Cell Biol.* **142**, 117-127. doi:10.1083/jcb.142.1.117

Martin, E., Girardello, R., Dittmar, G. and Ludwig, A. (2021). New insights into the organization and regulation of the apical polarity network in mammalian epithelial cells. *FEBS J.* **288**, 7073-7095. doi:10.1111/febs.15710

Michel, D., Arsanto, J. P., Massey-Harroche, D., Béclin, C., Wijnholds, J. and Le Bivic, A. (2005). PATJ connects and stabilizes apical and lateral components of tight junctions in human intestinal cells. *J. Cell Sci.* **118**, 4049-4057. doi:10.1242/jcs.02528

Morthorst, S. K., Nielsen, C., Farinelli, P., Anvarian, Z., Rasmussen, C. B. R., Serra-Marques, A., Grigoriev, I., Altelaar, M., Fürstenberg, N., Ludwig, A. et al. (2022). Angiomotin isoform 2 promotes binding of PALS1 to KIF13B at primary cilia and regulates ciliary length and signaling. *J. Cell Sci.* **135**, jcs259471. doi:10.1242/jcs.259471

Nagata, K. I. and Inagaki, M. (2005). Cytoskeletal modification of Rho guanine nucleotide exchange factor activity: identification of a Rho guanine nucleotide exchange factor as a binding partner for Sept9b, a mammalian septin. *Oncogene* **24**, 65-76. doi:10.1038/sj.onc.1208101

Nakajima, H. and Tanoue, T. (2011). Lulu2 regulates the circumferential actomyosin tensile system in epithelial cells through p114rhoGEF. *J. Cell Biol.* **195**, 245-261. doi:10.1083/jcb.201104118

Nakajima, H. and Tanoue, T. (2012). The circumferential actomyosin belt in epithelial cells is regulated by the Lulu2-p114RhoGEF system. *Small GTPases* **3**, 91-96. doi:10.4161/sgtp.19112

Odenwald, M. A., Choi, W., Buckley, A., Shashikanth, N., Joseph, N. E., Wang, Y., Warren, M. H., Buschmann, M. M., Pavlyuk, R., Hildebrand, J. et al. (2017). ZO-1 interactions with F-actin and occludin direct epithelial polarization and single lumen specification in 3D culture. *J. Cell Sci.* **130**, 243-259. doi:10.1242/jcs.188185

Olsen, O., Funke, L., Long, J., Fukata, M., Kazuta, T., Trinidad, J. C., Moore, K. A., Misawa, H., Welling, P. A., Burlingame, A. L. et al. (2007). Renal defects associated with improper polarization of the CRB and DLG polarity complexes in MALS-3 knockout mice. *J. Cell Biol.* **179**, 151-164. doi:10.1083/jcb.200702054

Otani, T. and Furuse, M. (2020). Tight junction structure and function revisited. *Trends Cell Biol.* **30**, 805-817. doi:10.1016/j.tcb.2020.08.004

Otani, T., Nguyen, T. P., Tokuda, S., Sugihara, K., Sugawara, T., Furuse, K., Miura, T., Ebnet, K. and Furuse, M. (2019). Claudins and JAM-A coordinately regulate tight junction formation and epithelial polarity. *J. Cell Biol.* **218**, 3372-3396. doi:10.1083/jcb.201812157

Penkert, R. R., Divittorio, H. M. and Prehoda, K. E. (2004). Internal recognition through PDZ domain plasticity in the Par-6-Pals1 complex. *Nat. Struct. Mol. Biol.* **11**, 1122-1127. doi:10.1038/nsmb839

Pieczynski, J. and Margolis, B. (2011). Protein complexes that control renal epithelial polarity. *Am. J. Physiol. Renal.* **300**, 589-601. doi:10.1152/ajprenal.00615.2010

Pombo-García, K., Martin-Lemaitre, C. and Honigmann, A. (2022). Wetting of junctional condensates along the apical interface promotes tight junction belt formation. *bioRxiv 2022.12.16.520750*.

Ran, F. A., Hsu, P. D., Wright, J., Agarwala, V., Scott, D. A. and Zhang, F. (2013). Genome engineering using the CRISPR-Cas9 system. *Nat. Protoc.* **8**, 2281-2308. doi:10.1038/nprot.2013.143

Roh, M. H., Makarova, O., Liu, C. J., Shin, K., Lee, S., Laurinec, S., Goyal, M., Wiggins, R. and Margolis, B. (2002a). The Maguk protein, Pals1, functions as an adapter, linking mammalian homologues of crumbs and discs lost. *J. Cell Biol.* **157**, 161-172. doi:10.1083/jcb.200109010

Roh, M. H., Liu, C. J., Laurinec, S. and Margolis, B. (2002b). The carboxyl terminus of zona occludens-3 binds and recruits a mammalian homologue of discs lost to tight junctions. *J. Biol. Chem.* **277**, 27501-27509. doi:10.1074/jbc.M201177200

Rouaud, F., Sluysmans, S., Flinois, A., Shah, J., Vasileva, E. and Citi, S. (2020). Scaffolding proteins of vertebrate apical junctions: structure, functions and biophysics. *Biochim. Biophys. Acta - Biomembr.* **1862**, 183399. doi:10.1016/j.bbamem.2020.183399

Schlüter, M. A., Pfarr, C. S., Pieczynski, J., Whiteman, E. L., Hurd, T. W., Fan, S., Liu, C. J. and Margolis, B. (2009). Trafficking of Crumbs3 during cytokinesis is crucial for lumen formation. *Mol. Biol. Cell* **20**, 4652-4663. doi:10.1091/mbc.e09-02-0137

Schulze, U., Vollenbröker, B., Braun, D. A., Van Le, T., Granado, D., Kremerskothen, J., Fränzel, B., Klosowski, R., Barth, J., Fufezan, C. et al. (2014). The Vac14-interaction network is linked to regulators of the endolysosomal and autophagic pathway. *Mol. Cell. Proteomics* **13**, 1397-1411. doi:10.1074/mcp.M113.034108

Schwayer, C., Shamipour, S., Pranjic-Ferscha, K., Schauer, A., Balda, M., Tada, M., Matter, K. and Heisenberg, C. P. (2019). Mechanosensation of tight junctions depends on ZO-1 phase separation and flow. *Cell* **179**, 937-952.e18. doi:10.1016/j.cell.2019.10.006

Shin, K., Straight, S. and Margolis, B. (2005). PATJ regulates tight junction formation and polarity in mammalian epithelial cells. *J. Cell Biol.* **168**, 705-711. doi:10.1083/jcb.200408064

Silver, J. T., Wirtz-Peitz, F., Simões, S., Pellikka, M., Yan, D., Binari, R., Nishimura, T., Li, Y., Harris, T. J. C., Perrimon, N. et al. (2019). Apical polarity proteins recruit the RhoGEF Cysts to promote junctional myosin assembly. *J. Cell Biol.* **218**, 3397-3414. doi:10.1083/jcb.201807106

Stevenson, B. R. and Begg, D. A. (1994). Concentration-dependent effects of cytochalasin D on tight junctions and actin filaments in MDCK epithelial cells. *J. Cell Sci.* **107**, 367-375. doi:10.1242/jcs.107.3.367

Straight, S. W., Shin, K., Fogg, V. C., Fan, S., Liu, C.-J., Roh, M. and Margolis, B. (2004). Loss of PALS1 expression leads to tight junction and polarity defects. *Mol. Biol. Cell* **15**, 1981-1990. doi:10.1091/mbc.e03-08-0620

Sun, D., Zhao, X., Wiegand, T., Bartolucci, G., Martin-Lemaitre, C., Grill, S. W., Hyman, A. A., Weber, C. and Honigmann, A. (2023). Assembly of tight junction belts by surface condensation and actin elongation. *bioRxiv 2023.06.24.546380*. doi:10.1101/2023.06.24.546380

Tan, B., Yatim, S. M. J. M., Peng, S., Gunaratne, J., Hunziker, W. and Ludwig, A. (2020). The mammalian crumbs complex defines a distinct polarity domain apical of epithelial tight junctions. *Curr. Biol.* **30**, 2791-2804.e6. doi:10.1016/j.cub.2020.05.032

Terry, S. J., Zihni, C., Elbediwy, A., Vitiello, E., San, I. V. L. C., Balda, M. S. and Matter, K. (2011). Spatially restricted activation of RhoA signalling at epithelial junctions by p114RhoGEF drives junction formation and morphogenesis. *Nat. Cell Biol.* **13**, 159-166. doi:10.1038/ncb2156

Thompson, B. J., Pichaud, F. and Röper, K. (2013). Sticking together the Crumbs-an unexpected function for an old friend. *Nat. Rev. Mol. Cell Biol.* **14**, 307-314. doi:10.1038/nrm3568

Umeda, K., Ikenouchi, J., Katahira-Tayama, S., Furuse, K., Sasaki, H., Nakayama, M., Matsui, T., Tsukita, S. S., Furuse, M. and Tsukita, S. S. (2006). ZO-1 and ZO-2 independently determine where claudins are polymerized in tight-junction strand formation. *Cell* **126**, 741-754. doi:10.1016/j.cell.2006.06.043

Van Itallie, C. M., Fanning, A. S., Bridges, A. and Anderson, J. M. (2009). ZO-1 stabilizes the tight junction solute barrier through coupling to the perijunctional cytoskeleton. *Mol. Biol. Cell* **20**, 3930-3940. doi:10.1091/mbc.e09-04-0320

Van Itallie, C. M., Tietgens, A. J., Krystofiak, E., Kachar, B. and Anderson, J. M. (2015). A complex of ZO-1 and the BAR-domain protein TOCA-1 regulates actin assembly at the tight junction. *Mol. Biol. Cell* **26**, 2769-2787. doi:10.1091/mbc.E15-04-0232

Van Rossum, A. G. S. H., Aartsen, W. M., Meuleman, J., Klooster, J., Malysheva, A., Versteeg, I., Arsanto, J. P., Le Bivic, A. and Wijnholds, J. (2006). Pals1/Mpp5 is required for correct localization of Crb1 at the subapical region in polarized Müller glia cells. *Hum. Mol. Genet.* **15**, 2659-2672. doi:10.1093/hmg/ddl194

Varelas, X., Samavarchi-Tehrani, P., Narimatsu, M., Weiss, A., Cockburn, K., Larsen, B. G., Rossant, J. and Wrana, J. L. (2010). The crumbs complex couples cell density sensing to hippo-dependent control of the TGF-β-SMAD pathway. *Dev. Cell* **19**, 831-844. doi:10.1016/j.devcel.2010.11.012

Wang, Q., Hurd, T. W. and Margolis, B. (2004). Tight junction protein Par6 interacts with an evolutionarily conserved region in the amino terminus of PALS1/stardust. *J. Biol. Chem.* **279**, 30715-30721. doi:10.1074/jbc.M401930200

Wang, Q., Chen, X. and Margolis, B. (2007). PALS1 regulates E-cadherin trafficking in mammalian epithelial cells. *Mol. Biol. Cell* **18**, 874-885. doi:10.1091/mbc.e06-07-0651

Weide, T., Vollenbröker, B., Schulze, U., Djuric, I., Edeling, M., Bonse, J., Hochapfel, F., Panichkina, O., Wennmann, D.-O., George, B. et al. (2017). Pals1 haploinsufficiency results in proteinuria and cyst formation. *J. Am. Soc. Nephrol.* **28**, 2093-2107. doi:10.1681/ASN.2016040474

Wells, C. D., Fawcett, J. P., Traweger, A., Yamanaka, Y., Goudreault, M., Elder, K., Kulkarni, S., Gish, G., Virag, C., Lim, C. et al. (2006). A Rich1/Amot complex regulates the Cdc42 GTPase and apical-polarity proteins in epithelial cells. *Cell* **125**, 535-548. doi:10.1016/j.cell.2006.02.045

Whiteman, E. L., Fan, S., Harder, J. L., Walton, K. D., Liu, C.-J., Soofi, A., Fogg, V. C., Hershenson, M. B., Dressler, G. R., Deutsch, G. H. et al. (2014). Crumbs3 is essential for proper epithelial development and viability. *Mol. Cell. Biol.* **34**, 43-56. doi:10.1128/MCB.00999-13

Yano, T., Tsukita, K., Kanoh, H., Nakayama, S., Kashihara, H., Mizuno, T., Tanaka, H., Matsui, T., Goto, Y., Komatsubara, A. et al. (2021). A microtubule–LUZP1 association around tight junction promotes epithelial cell apical constriction. *EMBO J.* **40**, e104712. doi:10.15252/embj.2020104712

Zihni, C., Mills, C., Matter, K. and Balda, M. S. (2016). Tight junctions: from simple barriers to multifunctional molecular gates. *Nat. Rev. Mol. Cell Biol.* **17**, 564-580. doi:10.1038/nrm.2016.80